Received: 18 March 2022 | Revised: 13 June 2022 | Accepted: 16 July 2022

DOI: 10.1002/aic.17842

AIChE JOURNAL

RESEARCH ARTICLE

Transport Phenomena and Fluid Mechanics

Study of trailing vortices and impeller jet instabilities of a flat blade impeller in small-scale reactors

Artemis-Danae Charalambidou[1] | Martina Micheletti[1] | Andrea Ducci[2]

[1]Department of Biochemical Engineering, University College London, London, UK

[2]Department of Mechanical Engineering, University College London, London, UK

Correspondence
Artemis-Danae Charalambidou, University College London, Department of Biochemical Engineering, Gower Street, London WC1E 6BT, UK.
Email: a.charalambidou@ucl.ac.uk

Funding information
Centre for Doctor-al Training (CDT) in Emerging Macromolecular Therapies, Engineering and Physical Sciences Research Council (EPSRC), Grant/Award Number: EP/L015218/1

Abstract

The design of economically feasible and profitable production processes has driven companies toward integrated continuous manufacturing by reducing working volumes and increasing operating frequencies. Thus, the development of robust small-scale devices capable of multivariate process optimization is essential. The aim of this work is to characterize the flow developed in a ml-scale stirred tank operating at intermediate Re ~3732, and assess trailing vortex stability with respect to baffle presence and size. Velocity characteristics are computed via computational fluid dynamics (CFD) and validated experimentally for an unbaffled (UB) and two baffled configurations. Proper orthogonal decomposition (POD) is used to extract dominant spatial–temporal flow features affecting the underlying flow patterns. Results show very good agreement between simulations and experiments, while POD analysis revealed the existence of highly energetic and periodic modes, linked to interactions between impeller jet and reactor walls. These modes are responsible for an impeller jet instability, which is amplified by the presence and size of baffles.

KEYWORDS
baffles, computational fluid dynamics, particle image velocimetry, POD, small-scale stirred tank reactor, trailing vortex

1 | INTRODUCTION

Stirred tank reactors (STRs) are widely used in the chemical, pharmaceutical and food processing industries in applications related to gas and/or solid–liquid dispersions, catalytic reactions and single or multiphase mixing.[1–3] Despite the versatility and flexibility of STRs, the flow generated during agitation consists of various temporal and spatial scales, which make the scale-up of mixing processes challenging and time-consuming. Specifically, in upstream processing, process characterization in STRs at lab-scale ranges from 1 to 20 L. The need for optimization of production lines and increase of throughput has led to the development of miniaturized STRs with working volumes between microliter to milliliter, which, operating in conditions similar to larger scale vessels, assist in refining the understanding of each step of the production process and provide a baseline for efficient and economically feasible scale-up.[4,5] Meanwhile, the aim for productivity maximization and automation has raised industrial interest toward continuous processing via high process intensification, reduction of working volumes and increase of operating frequencies.[6] Small-scale reactors are therefore valuable tools to test new impeller and vessel configurations and optimize operating conditions in a cost efficient and timely manner, contributing to the formation of robust and reliable manufacturing processes.

In agitated systems conversion of mechanical energy into momentum is significantly impacted by the impeller configuration which is critical for the hydrodynamic and mixing features developed

in the vessels.[2] In this regard, several studies have been dedicated to the investigation of novel impeller designs[2,7–10] or to the optimization of existing ones[11] by mainly focusing on the characteristics of the trailing vortices generated by each impeller, as the development and stability of the latter can control power consumption, dispersion and coalescence in gas–liquid mixing and ultimately determine reactor performance.[12]

To improve mixing performance and prevent solid body rotation, STRs operating with fluids of low viscosity are usually equipped with baffles. Still, there is a variety of applications in which the use of UB tanks is preferred, including crystallization and precipitation processes, where baffle presence may promote particle attrition.[13,14] UB vessels are also used in food and pharmaceutical industries where sterility and tank cleanness is of major importance, as well as in laminar mixing of high viscosity fluids, to prevent dead zones from forming in the proximity of the baffles.[14,15] Comparison between baffled and UB tanks along with flow dynamics and mixing characterization of STR performance with different baffle designs has been reported in the past.[16–20] Atibeni and Gao explored experimentally suspension mechanisms in STR equipped with up-triangular and down-triangular baffles and reported that the performance of the latter outweighed the standard baffle design exhibiting lower power consumption and critical agitation speed for particle suspension.[16] In previous years Lu et al. studied the dependency of mixing time on baffle number and size and mentioned that excessive baffling had an adverse effect on mixing efficiency.[17] Meaningful results on the flow stability were reported by Chapple and Kresta, who explored the effects of design parameters such as impeller type, off-bottom clearance and baffle number. According to their work, the most important parameters to determine flow stability at the impeller stream were impeller diameter, baffle number and interaction between the two.[18] In this perspective Roussinova et al. studied the flow instabilities occurring with an assortment of different axial impellers and a Rushton Turbine (RT) for varying number of baffles and concluded that reducing the baffle number triggers more flow instabilities in the case of the RT, rather than in axial impeller systems.[20]

Over the past years several studies have been conducted on the assessment of hydrodynamics to characterize mixing performance and operation efficiency of stirred tanks using both computational and experimental approaches. Recent experimental investigations on the flow dynamics in STRs have been mainly based on nonintrusive laser based/optical techniques, where the focus varied from the understanding of the flow in the bulk of the tank, on trailing vortices and flow instabilities[12,20–25] to quantifying turbulence levels and variation of local energy dissipation rate in proximity of the impeller, where micro-mixing plays a greater role.[22,26–29]

Computational fluid dynamics (CFD) has gained more attention during the last 20 years as it allows the investigation of multiple parameters for the prediction of flow patterns on single and multiphase systems.[30,31] Some studies investigated the impact of key design parameters in fluid flow, including the assessment of reactor and impeller geometry such as impeller clearance[32] and blade shape,[2,9] while others focused on the accuracy of different CFD models to predict STR flow.[33–37] Integration of experimental and computational methods is of major importance for the development of useful tools which, by combining the advantages of both approaches, provide deep insight on complex hydrodynamic phenomena. CFD is advantageous for revealing flow information at any point in the vessel volume and can fully resolve spatial and temporal scales of the flow but for high computational costs. In this perspective, experiments outweigh the limitations due to computational time but can only fully resolve all length scales in a flow for a small, mostly two-dimensional, investigation region and for a limited range of Reynolds number.[38]

While validation of CFD modeling has been discussed in the literature[35,39,40] the detailed characterization of hydrodynamics is limited to standardized reactor configurations with large (10–70 L) volumes and design ratios. However, the need for process efficiency and successful scale-up have rendered the characterization of ml-scale STRs critical to describe mixing and turbulence and identify potential bottlenecks associated with the process design.[7,41,42] Even though scale-down vessels are geometrically similar to larger scale systems, they can be significantly different in terms of operating conditions and process performance achieved. Scaling procedures in stirred tanks have been developed for chemical engineering applications with reactor sizes from 100 L onwards. Nevertheless, recent bioprocess development occurs for smaller working volumes (200 ml to 1 L); therefore scaling procedures should be tested in smaller scales, where the presence of probes and/or baffles can greatly affect the reactor hydrodynamics. Moreover, the matching of chemical processes in small and larger scales often results in altering critical operational parameters in the former (e.g., reduction in rotational speed), leading to lack of dynamic similarity and therefore flow regime across the different scales, with a transitional flow regime for the smaller scale systems considered.[43,44] These discrepancies are inevitable and further enhanced as reactor scales become smaller. Most scaling rules and design criteria have been adjusted and tested in fully turbulent conditions in large scale systems therefore alterations in flow regime in scale-down devices add extra challenges in hydrodynamics characterization that should be addressed for process optimization.[43]

Taking under consideration the aforementioned scaling issues between small and large scale upstream processes, a systematic characterization of engineering features in scale-down reactors is particularly important for the development of reliable scale-down models (SDMs) and has rarely been reported. Characterization of small-scale reactors has been limited to spatial distributions of ensemble-averaged flow quantities (i.e., mean velocity and turbulence) and estimation of power number.[43,44] The aim of this work is to fully assess the flow patterns developed in a small scale reactor, which has been actively used and optimized in continuous mode of operation by Tregidgo.[45] The vessel hydrodynamics at typical operating conditions are thoroughly characterized via CFD modeling and validated via particle image velocimetry (PIV) experiments. The impact of design parameters is assessed with a particular focus on baffle number and size, in order to evaluate the dependency of reactor hydrodynamics on key geometrical features. For this reason, three configurations of

the aforementioned scale-down reactor have been tested, one UB and two baffled configurations of increasing size. Finally, evolution of trailing vortices is characterized and their stability is correlated to highly energetic jet-instabilities, the effect and significance of which depends on the baffle presence and size. The acquired engineering and hydrodynamics knowledge provides a baseline to assess how critical design parameters affect the fluid dynamics in small scale reactors and can then be used to assist in the optimization of mixing, mass transfer, and scale-up.

2 | MATERIALS AND METHODS

2.1 | STR configuration

The STR used in the current work Figure 1A was a cylindrical SDM with a working volume of 250 ml. The vessel had a flat bottom with a diameter $D_T = 67$ mm, $H_L = 1.05D_T$ and was equipped with a six-blade flat blade turbine (FBT) with a diameter $D_i = 30$ mm ($D_i \sim 0.44D_T$), $w_b = 0.26D_i$, $t_{blade} = 0.05D_i$, and three equally spaced baffles. For the purposes of the current study, three STR configurations have been used: one unbaffled (UB) and two baffled configurations with baffles of equal thickness, $t_{baffle} = 0.5$ mm, but different widths, $D_T/16 = 4$ mm (B1) and $D_T/10 = 6.7$ mm (B2). The impeller clearance and rotational speed were 20 mm ($C \sim 0.3D_T$) and 250 rpm ($Re = ND_i^2\nu^{-1} = 3,732$), respectively. The working fluid was water with density $\rho = 998.2\,kg/m^3$ and dynamic viscosity $\mu = 0.001003\,kg/ms$. All experiments and simulations were conducted at room temperature.

2.2 | Experimental methods

All experiments were conducted in a cylindrical transparent vessel immersed in a rectangular trough made from acrylic, which minimized optical distortions caused by the curved surface of the cylindrical tank. This vessel is a transparent mimic of the scale-down STR used by Tregidgo for the optimization of perfusion processing.[45]

The 2D PIV time- and phase-resolved measurements of the instantaneous radial and vertical velocity components, u_r and u_z, were obtained on two different vertical planes located at different azimuthal distances from the baffles: the cross-section denoted as P1 in Figure 1A was 30° after the baffle, and cross-section P2 half way between two consecutive baffles. The plane of measurement was illuminated by a laser of thickness of approximately 1 mm in the measurement region and was obtained from a green diode-pumped solid state (DPSS) Laser with an output power of 500 mW. A 45° mirror was placed underneath the rig to redirect the laser vertically (Figure 1B). The working fluid was milli-Q water seeded with Rhodamine-coated Polymethyl methacrylate particles with an average diameter $d_p = 20 - 50\,\mu m$ and density $\rho_p = 1.19\,g/cm^3$ (Dantec Dynamics A/S). The 1MP intensified camera (Dantec Dynamics A/S), was equipped with a 45 mm lens and mounted an orange light cut-off filter with a wavelength of 570 nm, which allowed to maximize seeding particles detection and minimize laser reflection at the vessel and impeller surfaces. A sketch of the PIV setup is illustrated in Figure 1B.

Depending on the impeller speed and the tank region investigated (impeller vs. bulk tank regions) the frame rate varied from 2000 to 4000 Hz (time step size, $dt = 250 - 500$ ms). The results were post-processed via PIVlab 2.34 using an adaptive correlation analysis, with initial and final interrogation areas of 128×128 and 16×16 pixels^2, respectively, and 50% overlap (three-pass analysis). The spatial resolution used for the experiments was 1.1 mm, which is consistent with the order of magnitude of the Taylor microscale, $\lambda \sim 0.5 - 1$ mm, found in the literature[22,27] and estimated from CFD simulations, for $Re = 3732$ (see Section 2.3). Erroneous vectors were detected by applying velocity limits (approximately $\pm 2.5u_{tip} = 1\,ms^{-1}$) and discarding outliers with velocities five times greater than u_{tip}, that corresponded to ~2% of the generated vectors. Ensemble- and phase-averaged measurements were obtained from 4800 to 9600 instantaneous velocity

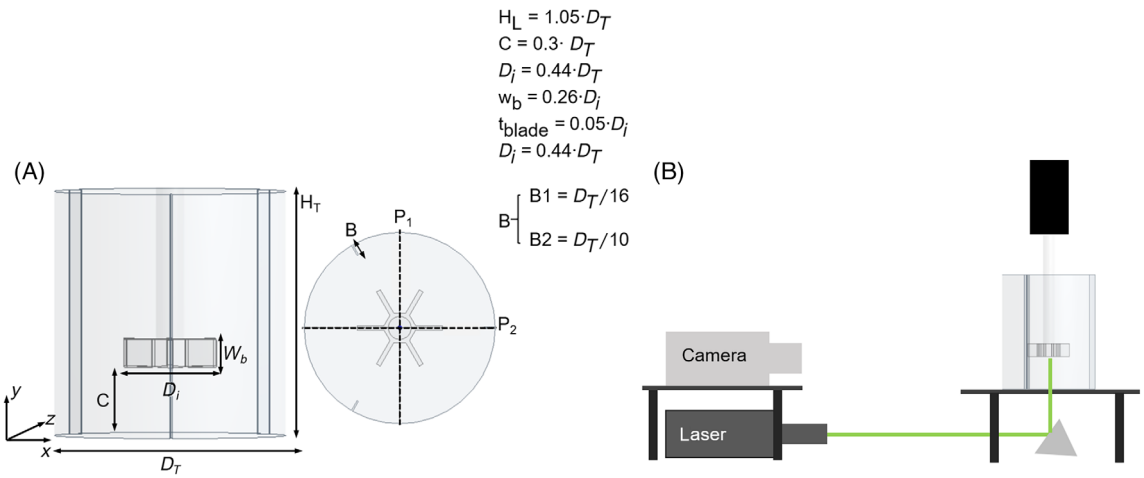

FIGURE 1 (A) Stirred tank configuration cross-section and plan view with indication of vertical measurement planes P1 and P2 and (B) experimental setup used for PIV

fields corresponding to 10 impeller revolutions, depending on the frame rate selected (500–250 μs), and 500 instantaneous velocity fields for each phase angle, respectively. Phase-resolved measurements were obtained with an angular resolution of 5°.

2.3 | Computational methods

The commercial CFD software ANSYS (version 19.2) was used to solve the flow governing equations inside the three scale-down STRs configurations studied (UB and baffled with B1 and B2). Reynolds averaged Navier–Stokes (RANS) modeling was employed to get an initial estimation of average and maximum values of turbulence kinetic energy (TKE) and flow length scales. These were then used to select an optimal spatial and temporal resolution of the Large Eddy Simulations (LES) performed to capture the flow characteristics in the three vessel configurations described above.

3 | RANS MODELING

3.1 | Mesh independence study

A mesh independence study was performed by using the stirred vessel configuration B1. The geometry was generated in ANSYS DesignModeler (version 19.2) and separated the reactor volume into two zones: moving and stationary. The moving zone enclosed the impeller and had a height of $2w_b$ and a diameter of $1.6D_i$. Five different unstructured mesh densities were assessed including 250, 600, 800, 900, and 1000 K elements. The simulations were conducted using the multiple reference frame (MRF) approach and the efficacy of the grid was evaluated based on velocity and turbulence distributions as well as the estimated power number, P_0 for the different mesh densities. The grid independence showed that increasing the grid size more than 900 K elements had marginal effect on velocity, turbulence distributions, and P_0. Therefore a grid of 900 K elements was used to conduct a sequence of simulations and screen the different RANS closure models to select the best precursor for LES.

3.2 | Estimation of turbulence length scales

Simulations were performed using a sliding mesh (SM) approach as it models more realistically impeller rotation and accounts for transient interactions between impeller and baffles.[34,36,37] The time step used corresponded to 1° angular displacement ($dt = 6.66 \cdot 10^{-4}$ s) that kept cell convective courant number <1 for the entire volume of the tank.[35] According to the predicted average dissipation rate, ε, and turbulent kinetic energy, k, the order of magnitude of the integral, Taylor and Kolmogorov length scales were $\overline{l_o} \propto 10^{-3}$m, $\overline{\lambda} \propto 10^{-4}$m, and $\overline{\eta} \propto 10^{-5}$m, respectively.[22,27] Their average value was used to pick an adequate grid spatial resolution for the conduction of LES. Maximum energy dissipation rate, ε_{max}, was also used to compute the Kolmogorov timescale and therefore refine the temporal resolution of the LES in the impeller region.[44] The simulation conditions and the different approaches used are summarized in Table 1.

Double precision was used to perform all RANS simulations. A pressure-based implicit solver was applied and a second order upwind scheme was used for spatial discretization of continuity and momentum equations. SIMPLEC algorithm was used for pressure–velocity coupling. Convergence was evaluated based on residuals being $<10^{-6}$ for continuity and momentum and 10^{-5} for turbulence. Other physical convergence criteria included monitoring the velocity at different points in the vessel, average turbulence in the impeller rotational area and the momentum of the shaft.

3.3 | LES modeling

The second set of CFD simulations was conducted by using LES. When using LES, the Navier–Stokes equations are filtered and solved up to large turbulence scales within a certain cut-off grid size, beyond which smaller turbulence scales (subgrid scales) are assumed to be isotropic and are modeled via a subgrid scale model (Equations (3) and (4)). The filtered Navier–Stokes equations are:

$$\frac{\partial \overline{u}_i}{\partial x_i} = 0 \tag{1}$$

$$\frac{\partial \overline{u}_i}{\partial t} + \frac{\partial}{\partial x_j}\left(\overline{u}_i \overline{u}_j\right) = -\frac{1}{\rho}\frac{\partial \overline{p}}{\partial x_i} + \nu \frac{\partial^2 \overline{u}_i}{\partial x_j^2} - \frac{\partial \overline{\tau_{ij}^{SGS}}}{\partial x_j} \tag{2}$$

$$\tau_{ij}^{SGS} = -\nu_T\left(\frac{\partial \overline{u}_i}{\partial x_j} + \frac{\partial \overline{u}_j}{\partial x_i}\right) \tag{3}$$

$$\nu_T = C_s \Delta \sqrt{\frac{1}{2}\left(\frac{\partial \overline{u}_i}{\partial x_i} + \frac{\partial \overline{u}_j}{\partial x_j}\right)} \tag{4}$$

In this work, Smagorinsky model was used which is an eddy-viscosity model relating the subgrid-eddy viscosity, ν_T, to the resolved deformation rate (Equation (4)). The filtering process in Fluent is determined from the grid spacing, Δ, therefore turbulence scales larger than the grid size are fully resolved, whereas smaller turbulence scales are modeled. The Smagorinsky constant used in this study was $C_s = 0.1$, which is typical for turbulent flows[46] and in agreement with previous studies of Delafosse et al., who did not find significant variation in velocity and TKE distribution between $C_s = 0.1$ and $C_s = 0.2$.[35] The selected value of C_s is also in agreement with Gillisen et al. (2012) who compared results between LES and direct numerical simulations (DNS) and found out that $C_s = 0.1$ was suitable for both mean velocity and turbulence prediction.[47]

The final grid used for LES consisted of 3 million tetrahedral elements with spatial resolution $7\,\mu m < \Delta x < 1.8$ mm. In agreement with Hartmann et al.[39] the ratio of eddy viscosity over kinematic viscosity (ν_T/ν) was monitored during the course of the simulation to ensure

TABLE 1 Summary of the different conditions used across the different steps of the simulation process

CFD simulation	Steady state (MRF)/transient simulation (sliding mesh)	Mesh size (number of elements)	Model	Purpose
RANS	Steady state (MRF)	250–1000 K	k–ε Realizable	Mesh independence
URANS	Transient (sliding mesh)	900 K	k–ε Standard, k–ε Realizable, k–ε RNG, Reynolds stress model (RSM)	Screening of URANS models
URANS	Transient (sliding mesh)	3 M	k–ε Realizable	LES precursor
LES	Transient (sliding mesh)	3 M	Smagorinsky model ($C_s = 0.1$)	LES simulation/results extraction

that the grid quality was good enough to successfully resolve a large range of turbulence length scales and minimize the amount of modeling occurring within the subgrid scale. The resulting ratio in the sliding mesh region had an average value of $\nu_T/\nu \sim 20\%$ indicating adequate spatial resolution as almost 80% of the flow field was appropriately resolved and only 20% was modeled.

SIMPLEC algorithm was used for pressure–velocity coupling and Bounded Central Differencing scheme for spatial discretization of momentum. Convergence was monitored based on residual values being $<10^{-5}$ for momentum equations, while additional criteria included the statistical convergence of velocity magnitude in points in and out of the rotational area. Impeller momentum was also monitored during the course of LES to ensure convergence was reached. The time step size was selected to be $dt = 3.3386 \cdot 10^{-4}$ s, lower than the Kolmogorov timescale estimated from URANS simulations ($\tau_K = (\nu/\bar{\varepsilon})^{0.5} \propto 10^{-3}$ s) corresponding to an angular displacement of $d\varphi \sim 0.5^{\circ}$ and ensuring the Courant number was below unity in the whole reactor volume. Forty revolutions have been simulated for the UB and the baffled configurations equipped with B2, and 80 revolutions for the baffled case equipped with B1. For all configurations the first 20 revolutions were performed to ensure simulation statistical convergence and the remaining 20 (UB and baffled with B2), and 60 revolutions (baffled with B1), were used for data acquisition and processing. This corresponds to 14,400 instantaneous acquisitions for the UB and the B2 vessel configurations. For the baffled configuration B1, the simulation time was extended to 60 revolutions (~43,200 acquisitions) as this was the standard vessel configuration designed and tested by Tregidgo.[45]

3.4 | Processing methods

3.4.1 | Velocity and turbulence data

The post processing of calculated velocity fields was conducted in MATLAB. A regular space grid of $[dx, dz] = 0.7$ mm was used to map the unstructured computational grid and its order of magnitude was consistent with the grid originated experimentally. The generated grid agreed with the minimum cell size from ANSYS meshing and was of the same order of magnitude of the estimated Kolmogorov microscale.

LES Phase resolved velocity fields were estimated from 120 and 360 instantaneous fields corresponding to blade positions of $\varphi = 0^{\circ} - 60^{\circ}$. Statistical averaging over all impeller blade positions (i.e., 0°–60°, with a temporal resolution corresponding to angular displacement of 0.5°) was used to compute ensemble-averaged quantities.

Given the 2D nature of the PIV system used in the present work the contribution to the TKE due to velocity fluctuations in the tangential direction was included in $\overline{k'}$ by assuming pseudo-isotropic flow. This is consistent with the works of Zhao et al. (2011) and Khan et al. (2006), who demonstrated that this assumption is valid for fully baffled STR flows and turbulent kinetic energy estimates are only marginally affected.[3,48]

3.4.2 | Proper orthogonal decomposition and frequency analysis

Proper orthogonal decomposition (POD) has been employed to identify dominant frequencies and flow structures in a broad range of flow fields.[49,50] It is a linear technique which allows to decompose an instantaneous flow snapshot into a number of spatial and temporal modes of descending kinetic energy magnitude. The first modes therefore contain most of the kinetic energy embedded in the flow and are linked to larger scale structures, as opposed to lower order modes which have less kinetic energy and are associated with smaller scales and turbulence. Once dominant modes are identified, POD allows to produce low order models (LOMs) which can be used to substantially reduce the dimension of the dataset, and therefore isolate flow instabilities.[26,50] In this work, POD was used with the method of snapshot, with matrix X being characterized by R rows, corresponding to spatial variation in the radial and axial directions, and M columns, corresponding to the number of frames used either from the PIV experiments or LES. When using the POD modes an instantaneous velocity field, $\boldsymbol{u_i}$, can be written as follows (Equation (5)):

$$\boldsymbol{u_i}(\boldsymbol{x}, t) = \sum_{n=1}^{n=M} a_n(t)\boldsymbol{\Phi_n}(\boldsymbol{x}) \tag{5}$$

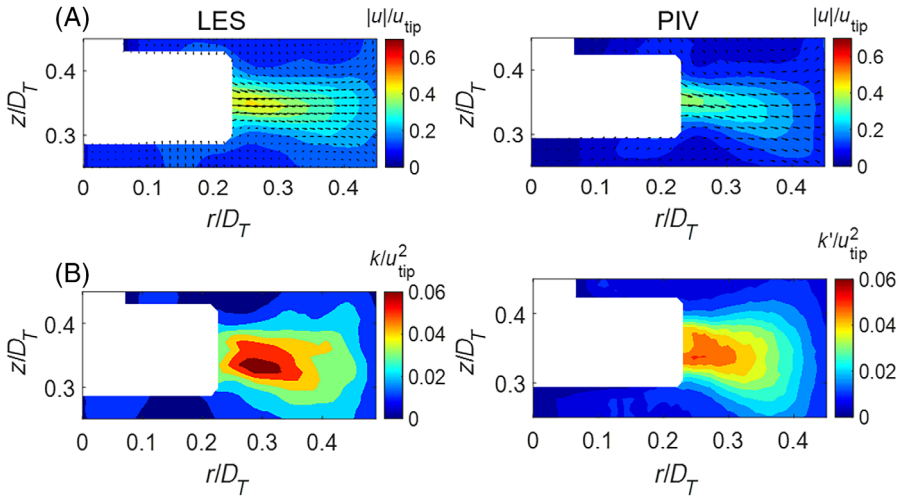

FIGURE 2 Experimental–numerical validation: (A) of ensemble average velocity magnitude and (B) TKE for PIV and LES for a vertical plane in the UB tank

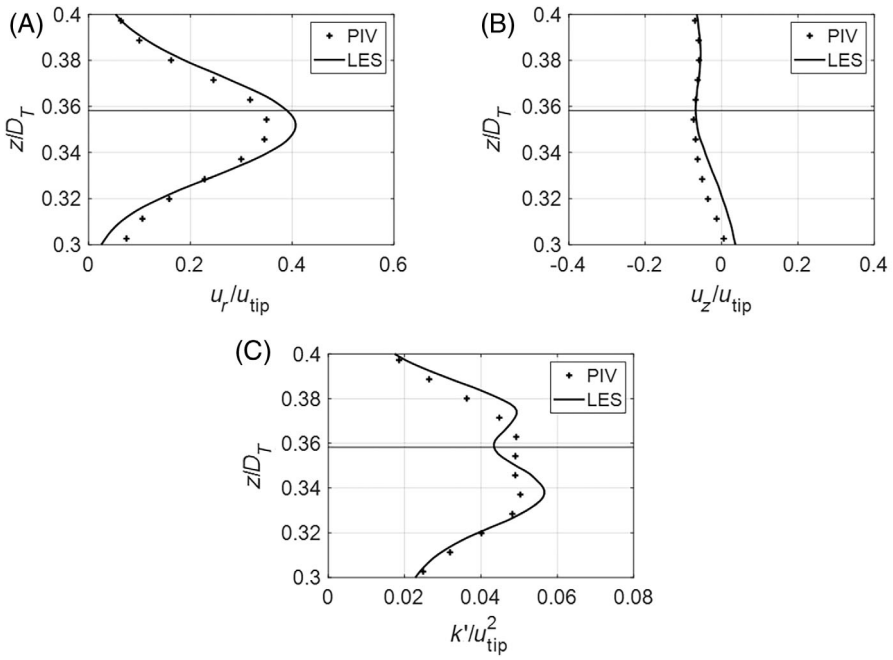

FIGURE 3 Vertical profiles of ensemble average quantities: (A) u_r/u_{tip}, (B) u_z/u_{tip}, and (C) k'/u_{tip}^2 at $r/D_T = 0.25$ for the UB tank. The solid horizontal line in all figures represents the impeller centerline

where $a_n(t)$ is the temporal coefficient and $\boldsymbol{\Phi_n}(\boldsymbol{x})$ is the spatial eigenfunction associated with the nth mode. More details on the method can be found in the literature.[26,38,50–52]

4 | RESULTS AND DISCUSSION

4.1 | Validation of CFD

The LES velocity fields were validated against corresponding PIV results for all the configurations investigated (UB, B1, and B2). For brevity of presentation, contour-maps and velocity profiles are presented for the unbaffled vessel only on a vertical plane. Consistent agreement was also found for the configurations with baffles. Contour maps of ensemble averaged velocity magnitude and turbulent kinetic energy are illustrated in Figure 2, while vertical profiles of ensemble averaged radial, u_r/u_{tip}, axial, u_z/u_{tip}, velocity components and turbulent kinetic energy, k'/u_{tip}^2, are presented for a radial position in proximity to the impeller tip, $r/D_T = 0.25$, where maximum velocities and TKE levels occur (Figure 3A–C, respectively). The agreement for axial velocity components and turbulent kinetic energy estimates is good, with an error within 4%, while the peak for the radial velocity component is slightly underestimated, by approximately 15%, from the corresponding PIV measurement. This discrepancy could be caused by the fact that ensemble averages were estimated experimentally with a coarser angular resolution (i.e., it consists in an average of only 12 phased resolved datasets), while LES had a finer angular resolution of 0.5°, which included the entire range of velocity fields in between two blade passages. Vertical profiles of the phase-resolved radial and axial velocity components, $\langle u_r \rangle/u_{tip}$ and $\langle u_z \rangle/u_{tip}$, are presented for different impeller phase angles and for radial positions in close proximity to

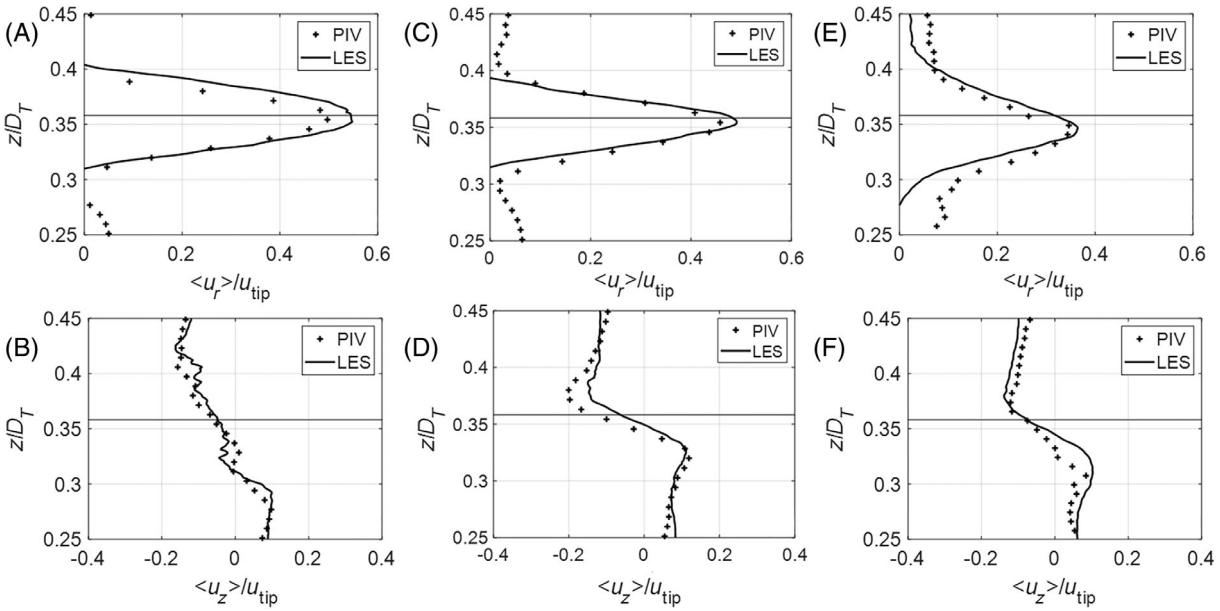

FIGURE 4 Vertical profile of $\langle u_r \rangle / u_{tip}$ (A, C, and E) and $\langle u_z \rangle / u_{tip}$ (B, D, and F) for the UB tank: (A, B) $\varphi = 10^{\circ}$ and $r/D_T = 0.22$; (C, D) $\varphi = 30^{\circ}$ and $r/D_T = 0.25$; (E, F) $\varphi = 50^{\circ}$ and $r/D_T = 0.27$. The solid horizontal line represents the impeller centerline

the trailing vortex core ($r/D_T = 0.22$ at 10°, $r/D_T = 0.25$ at 30°, $r/D_T = 0.27$ at 50°), in Figure 4. Vertical profiles of $\langle u_r \rangle / u_{tip}$ show that radial velocity reaches a maximum at 10° behind the blade, when the trailing vortices have fully formed. As the blade progresses and the intensity of the trailing vortices weakens, the radial velocity, $\langle u_r \rangle / u_{tip}$, gets progressively smaller as well. Similarly, vertical profiles of $\langle u_z \rangle / u_{tip}$ indicate very good agreement between the PIV and LES phased resolved estimates.

Average velocity and TKE values were compared with previously published results for all reactor configurations studied, including baffled and unbaffled.[1,39,40,48,53] It should be noted that the impeller geometry used in this work is different from impeller configurations extensively examined in the past, such as the commonly used RT[1,22,40] or four-blade FBT.[7,54] For an unbaffled configuration as in this work, Alcamo et al. investigated the flow produced by a RT for $Re = 30,000$ and found maximum values of radial component, $u_r/u_{tip} = 0.22$ and turbulent kinetic energy $k'/u_{tip}^2 = 0.05$ close to those found in the current work.[1] The work of Steiros et al. with an octagonal unbaffled tank and a four blade FBT was denoted by higher levels of turbulence (turbulence intensity $\sqrt{\langle u_r^2 \rangle + \langle u_z^2 \rangle}/u_{tip} \sim 0.45$ vs. 0.24 in the current work), as the corner of the prism wall might have resulted in a baffle effect.[7] As expected, when baffled configurations are considered turbulence levels are increased. For example, Lee et al. and Hartmann et al., reported higher values for TKE than those found in the current work ($k'/u_{tip}^2 = 0.15$ vs. 0.4).[39,55] Nevertheless, differences related to impeller design, reactor volumes (ranging from 5 to 70 L) and flow regime ($Re \sim 10,000 - 150,000$) must be considered when comparing the current and their configurations and highlights the demand of a thorough characterization for both baffled and unbaffled configurations of small volume STRs.

4.2 | Comparison of UB and baffled configurations

4.2.1 | Profiles of velocity and turbulence

A direct comparison between the flow characteristics of the three configurations, UB, B1, and B2 investigated is provided in Figure 5 where the contour maps of in-plane velocity magnitude and TKE, extracted from LES data, are illustrated. The in-plane velocity magnitude is higher in the presence of baffles and increases with larger baffle size. This is expected as for UB vessels the flow is more subject to solid body rotation and the main velocity component under this condition is the tangential one, which is not accounted for in the contour maps of Figure 5. Baffles transfer energy from the tangential to the axial and radial velocity components, resulting in larger and more effective upper circulation loops. For example at $\varphi = 40^{\circ}$, the upper loop reaches a maximum axial coordinate of $z/D_T = 0.63$ and $z/D_T = 0.6$ for B2 and B1 configurations, respectively. Similarly, TKE is found to increase threefold with the addition of baffles and with baffle size as shown in Figure 5. In the unbaffled case, the low impeller pumping capacity caused by the increased circumferential motion, leads to a P_0 which is 2.5 times lower when compared with baffled tank B2 and consequently to the lower turbulence levels observed.

4.2.2 | Characterization of trailing vortices

Considering the impact of the trailing vortices on the STRs overall flow and mixing performance, a thorough characterization of their formation and stability has been conducted in the following part of this work.

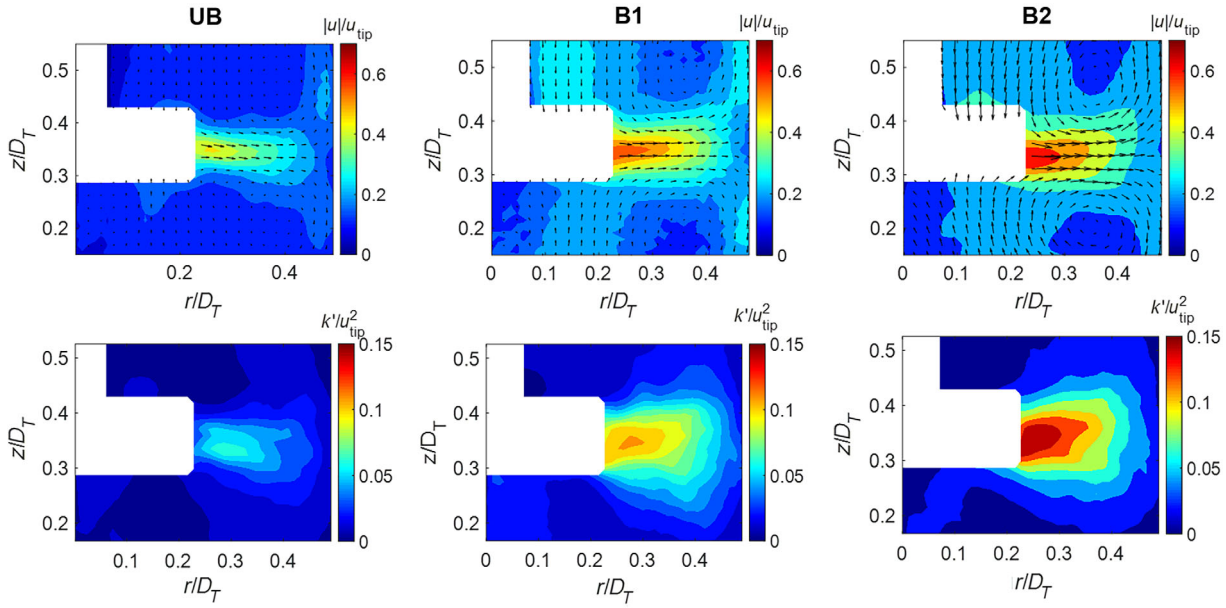

FIGURE 5 Comparison of velocity magnitude and TKE distributions for the UB, and baffled configurations (LES data at plane of measurement P1)

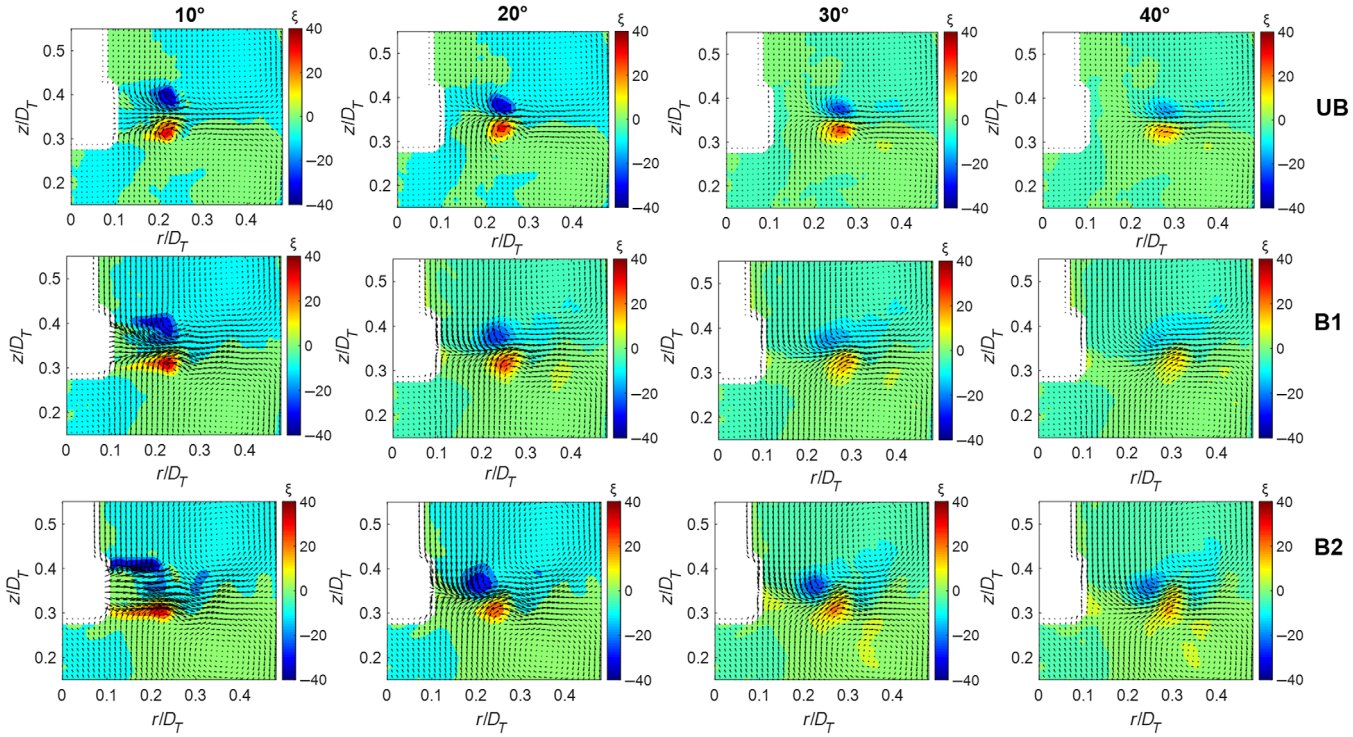

FIGURE 6 Contour map of normalized vorticity for UB and baffled configurations (B1 and B2 at plane P1) for phase angles ranging $\varphi = 10^{\circ} - 40^{\circ}$. Results presented correspond to LES dataset

The phase-resolved vector field and corresponding tangential vorticity ($\xi = H_L\langle\omega_\theta\rangle/u_{tip}, u_{tip} = \pi N D_i$) contour map is shown in Figure 6, based on LES data, for four different angles behind the blade ($\varphi = 10^{\circ}, 20^{\circ}, 30^{\circ}$, and 40°) and for all the three configurations UB, B1, and B2. In the unbaffled vessel the trailing vortices are clearly developed with nearly equal vorticity of opposite magnitude on either side of the impeller centerline. The two vortices are parallel and move radially outwards as the phase angle, φ, increases. The addition of the smaller baffles B1 in the system introduces an inclination of the jet in between the vortex pair, which is increasing as the phase

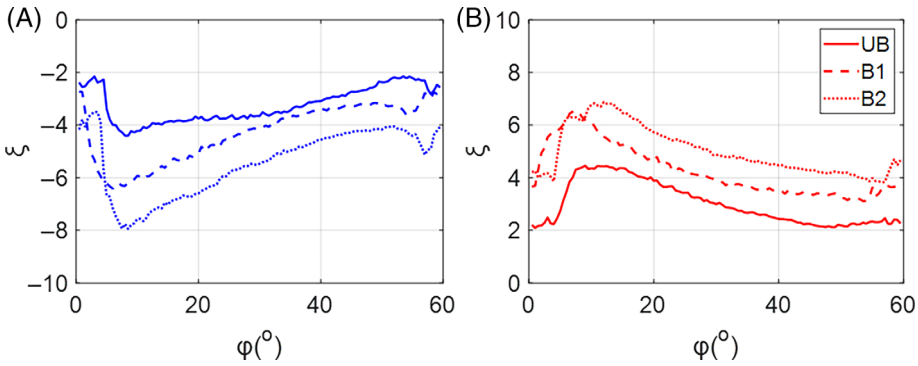

FIGURE 7 Vorticity level based on local spatial averages of LES data at plane P1 for the UB (continuous line) and baffled configurations, B1 (Dashed line), and B2 (Dotted line): (A) upper vortex and (B) lower vortex

angle is increased. The jet inclination, β, is quantified based on Equation (6) inside an area with dimensions $0.2 < r/D_T < 0.43$ and $0.23 < z/D_T < 0.45$ on the vertical plane of measurement (either P1 or P2) for each configuration (i.e., UB, B1, and B2). For example, the centerline jet inclination, β, computed from Equation (6) for B1, is found to reach approximately 4° when $\varphi = 10^{\circ}$ and ~5° when $\varphi = 40^{\circ}$, while it is ~0° for the unbaffled case. This effect is even more pronounced for the larger baffle configuration, B2, where the jet inclination increases to $\beta \sim 5^{\circ} - 7^{\circ}$ for $\varphi = 10^{\circ} - 40^{\circ}$. Besides the inclination of the vortex pair and their central jet, the presence of baffles causes a more prominent radial movement of the bottom vortex as opposed to the top one. For example, in the B1 configuration the radial position of the bottom vortex ranges from $r/D_T = 0.22$ to $r/D_T = 0.32$, as opposed to the UB vessel where the radial distance covered from the same vortex is $r/D_T = 0.22$ to $r/D_T = 0.27$ when $\varphi = 10^{\circ} - 40^{\circ}$. These two effects, that is, increased jet inclination and more prominent radial movement of the bottom trailing vortex, might be related to a reduction in trailing vortices stability as the blade progresses.

$$\beta(\varphi, t) = atan^{-1}\left(\frac{u_z}{u_r}\right) \tag{6}$$

In Figure 7 a comparison of vorticity levels is shown across the three vessel configurations studied in this work. The intensity of the trailing vortices has been estimated from the average vorticity, processed from LES data, in proximity to the blade in a region comprised between $r/D_T = 0.2 - 0.4$. For all vessel configurations the maximum absolute vorticity magnitude occurs when $\varphi \sim 12^{\circ}$. In the UB tank the peak is at $\varphi = 9^{\circ}$ while it shifts to angular positions further away from the blade, $\varphi = 10^{\circ}$ and 12°, in baffled tank configurations, B1 and B2, respectively. Furthermore, the intensity of both vortices (upper and lower) increases in magnitude as configurations with baffles are considered with B2 being characterized by a nearly double absolute vorticity peak, when compared with the UB configuration (i.e. 8 vs. 4 for top vortex). Such behavior is expected as both phase-resolved vorticity magnitude and area covered by the trailing vortices appear to be larger in the B2 vessel. Finally, when comparing the upper and lower vortices for the B2 configuration, it is clear that there is an imbalance between the two, and the magnitude of the top vortex is nearly 17% higher than the bottom one, as opposed to the UB and B1 configurations where the two trailing vortices exhibit similar magnitudes.

4.2.3 | Analysis of impeller jet inclination

To further elucidate the trailing vortices dynamics, instantaneous velocity vector plots ($\boldsymbol{u_i}(\varphi, t)$) denoted by the maximum and minimum inclination of the jet between the vortex pair are provided in Figure 8 for all the configurations investigated. The vector maps, shown in Figure 8 include both LES (Figure 8A) and PIV (Figure 8B) datasets and are all related to a phase angle $\varphi = 10^{\circ}$ at different time instants, when the trailing vortex cross-section is fully visible to the side of the blade. It is interesting to note that these large deflections of the impeller jet are only partially captured in the phase resolved data at $\varphi = 10^{\circ}$, and are most likely to be more pronounced at larger phase angles where the imbalance between the two trailing vortices in the phase resolved vector maps is higher (Figure 6).

To quantify the amount of jet fluctuation and identify potential frequencies related to this phenomenon, the angle of the jet in proximity to the impeller blade was estimated based on the ratio between the axial and radial velocity components (Equation (6)), in a window with dimensions $0.2 < r/D_T < 0.43$ and $0.23 < z/D_T < 0.45$ on the vertical plane of measurement for each configuration studied. The size of this area, where β was calculated, was based on the location of trailing vortices (Figure 6) as well as the jet inclination observed in the instantaneous velocity vector plots (Figure 8) and its use for the calculation of the angle of the jet was consistent across all vessel configurations for both simulations and experiments. The results presented in Figure 9 are based on instantaneous velocity phase-resolved datasets obtained for $\varphi = 10^{\circ}, 30^{\circ}$, and 50° from PIV, that is, 500 frames corresponding to 500 revolutions of the impeller, for plane P1. To improve the readability of the data, the solid black reference line was obtained through a moving average, applied to smooth the dataset. For the unbaffled vessel, and for $\varphi = 10^{\circ} - 50^{\circ}$, it is evident that the fluctuations of the jet inclination are minimal, as the smoothed reference line marginally fluctuates around 0°. For the baffled tanks, the fluctuations are more pronounced with inclination of the reference black line varying between ±19°. Moreover, in the presence of baffles the jet inclination fluctuations are characterized by a periodic behavior with a period ranging from 37 to 47 ($\sim 0.087\,\text{Hz} < f < 0.11\,\text{Hz}$) revolutions and 57 to 68 ($\sim 0.06\,\text{Hz} < f < 0.073\,\text{Hz}$) revolutions for the B1 and B2 vessel configurations, respectively. The amplitude of the fluctuation increases as larger phase angles are considered for both B1 and B2 cases. For example, when considering the B1 configuration the

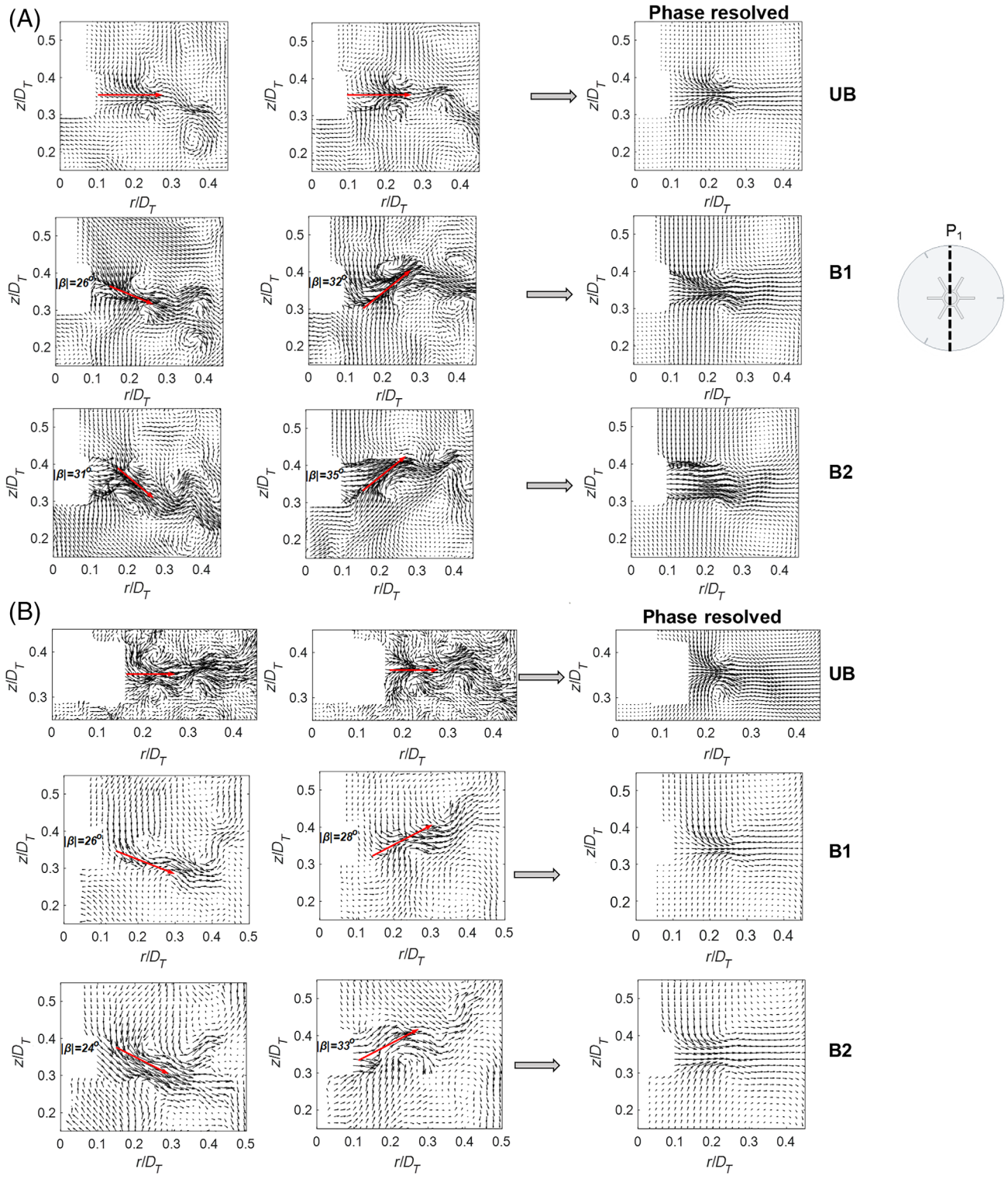

FIGURE 8 Instantaneous $(\boldsymbol{u}_i(\varphi,t)/u_{\text{tip}})$ and phase resolved $\langle u_i\rangle/u_{\text{tip}}$ velocity vector plots for $\varphi = 10^{\circ}$ and for plane P1: (A) LES and (B) PIV

amplitude of the reference line is 9°, 12°, 16° for $\varphi = 10^{\circ}, 30^{\circ}$, and 50°, respectively, indicating that the instability is greater further away from the blade.

To study whether the oscillation amplitude and frequency was affected by the location of the baffles, the variation of the angle of the jet is shown in Figure 10 for configuration B1 on the plane P2, in proximity of the baffle, for both experiments and simulations. When comparing Figures 9 and 10 it is clear that the same jet periodicity is occurring for the experimental data on both planes P1 and P2, with a frequency of ~37–47 revolutions which corresponded to

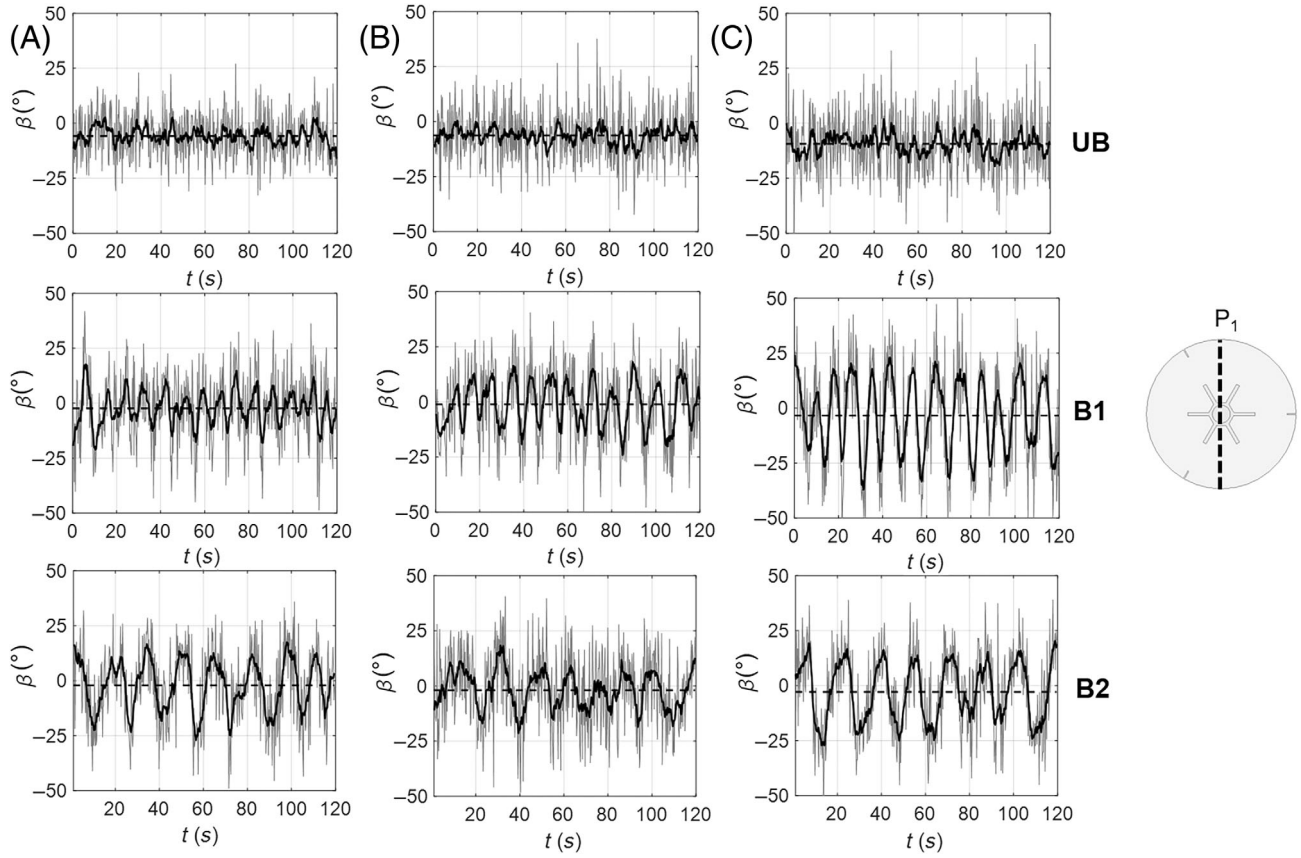

FIGURE 9 Variation of the angle of the jet, β, at plane P1 for the B1 and B2 configurations. The jet angle was estimated from phase-resolved PIV data (every revolution) for phase angle: (A) $\varphi = 10^{\circ}$, (B) $\varphi = 30^{\circ}$, and (C) $\varphi = 50^{\circ}$

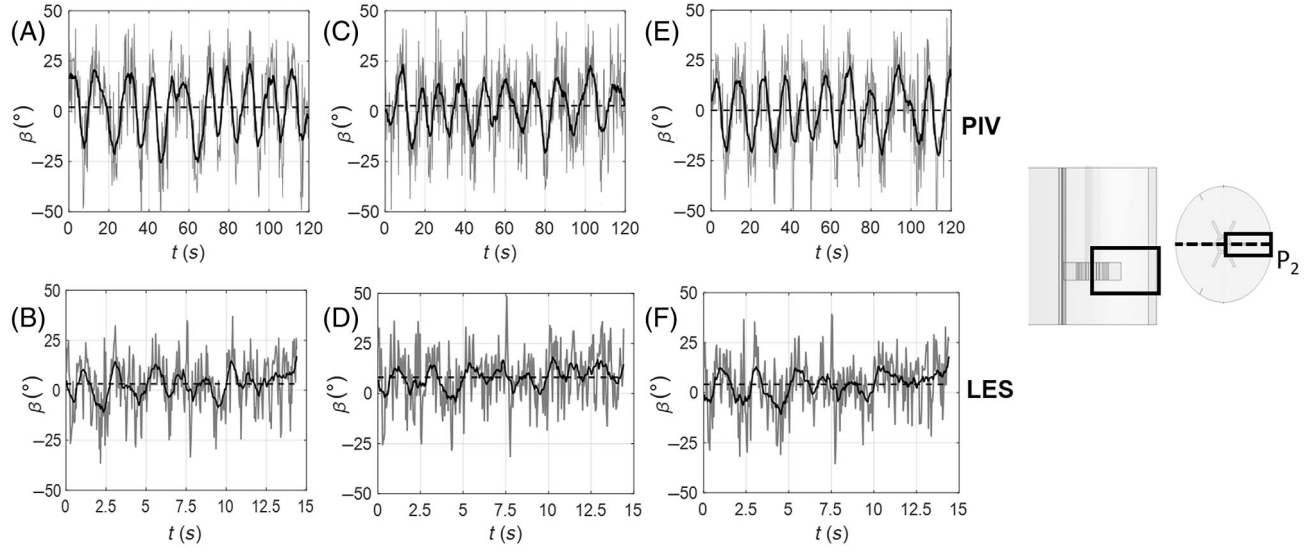

FIGURE 10 Variation of the angle of the jet, β, at plane P2 for the B1 configuration. The jet angle was estimated from phase-resolved PIV (every revolution) and LES (every impeller passage) data for phase angles $\varphi = 10^{\circ}$ (A and B), 30° (C and D), and 50° (E and F)

$f \sim 0.087 - 0.11$ Hz, while the amplitude of oscillation is slightly higher in the P2 plane, where β ranges from 17°–19° at $\varphi = 10^{\circ}, 30^{\circ}$, and 50°. To investigate whether the frequency of the jet fluctuation was consistent between the simulations and phase-resolved PIV measurements, the time resolved 60-revolutions long LES dataset was further analyzed for the B1 configuration. In this case, the angle of the jet was estimated per blade passage on the measurement plane P2 (taking into account 360 positions in total for each angle φ, that is,

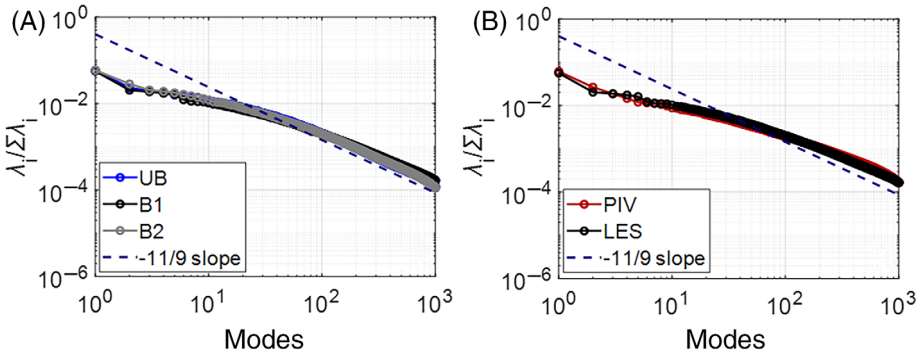

FIGURE 11 POD eigenvalue spectrum: (A) from LES for the three vessel configurations (UB and baffled with B1 and B2 at plane P2) and (B) for B1 baffled tank from PIV and LES data (P2 plane)

every 60° for 60 revolutions) and is illustrated in Figure 10. The estimated jet instability provided a peak to peak period of 8–10 impeller revolutions and corresponded to a frequency of $f \sim 0.4 - 0.5$ Hz, four times higher than the one observed experimentally. The higher frequency values arisen from the LES can be related to the limited simulation time compared with the experiments (15 vs. 120 s) which is not long enough to fully resolve an instability characterized by such a low frequency ($f \sim 0.087 - 0.11$ Hz). To elucidate these discrepancies, the flow fields for the UB and B1 configurations were further investigated via POD and Fast Fourier Transform (FFT) analyses for both experimental and computational datasets.

4.2.4 | POD analysis and flow reconstruction

To better understand the dynamics and nature of the jet instabilities and assess the periodicity of the oscillating frequency, POD was applied to the time-resolved LES and PIV data, for all the vessel configurations. The percentage contribution of each mode to the total kinetic energy spectrum is illustrated in Figure 11A,B where the modal energy is directly related to the corresponding eigenvalue. To consistently compare PIV and LES data, velocity decomposition was conducted considering only velocity components in the axial and radial direction. The first mode contains most of the energy of the system (~6%) for all three configurations. This mode corresponds to the ensemble averaged flow field (i.e., the mean flow was not subtracted from the data set prior to applying POD). The most significant contribution to the total energy is observed from the first five modes as they appear to represent ~25% of the total energy. Modes of higher order (roughly after mode 10) tend to follow a −11/9 slope, denoted by the dash blue line in Figure 11, which can be used as a reference to identify the range of modes corresponding to the turbulent inertial subrange.[56] Comparison of the eigenvalue spectrum produced by LES and PIV in Figure 11B shows good agreement between simulations and experiments and highlights that the current LES data is sufficiently resolved to correctly identify the turbulent inertial subrange. Previous CFD works based on RANS simulations which attempted to resolve the energy spectrum via POD, were denoted by a discrepancy with experimental results with a steep decline of the energy content in the range of modes associated with the inertial subrange.[38]

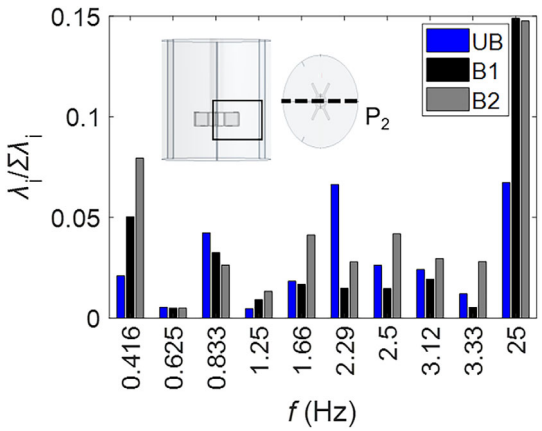

FIGURE 12 Cumulative eigenvalue contribution associated with the peak frequencies found after performing FFT analysis of POD modes from LES dataset (P2 plane of measurement)

FFT was performed to the temporal coefficient $a_n(t)$ to find dominant frequencies of the POD modes. A visualization of the energy content of the frequencies most commonly found in the three different tank configurations after conducting LES is illustrated in the bar plot in Figure 12. The total energy of each frequency was computed by adding the energy associated with those modes, which exhibited the same dominant frequency after applying FFT on the temporal eigenfunction. As expected for each reactor type, the frequency with the highest energy corresponds to the blade passage frequency (BPF), $f_{BPF} = 25$ Hz which is inherently linked to the periodic fluctuations and organized motion of the flow in proximity of the impeller. The next high energy content frequency, which is related to the second group of most energetic modes, corresponds to $f_{Baffled,LES} = 0.416$ Hz and $f_{UB,LES} = 2.29$ Hz for the baffled (with B1 and B2) and unbaffled configurations, respectively. Interestingly the second POD mode was always associated with those dominant frequencies identified for each configuration (i.e., 0.416 Hz for baffled and 2.29 Hz for UB).

To further elucidate the velocity fields and energy spatial distribution of the modes associated with those frequencies, the mode magnitude, $\sqrt{(\Phi_r(x))^2 + (\Phi_z(x))^2}$, is presented in Figure 13. Figure 13A illustrates the spatial eigenfunction of the first mode for both unbaffled and baffled reactors. As the first mode corresponds to the mean flow field, it captures most of the variance and is structurally similar to the ensemble

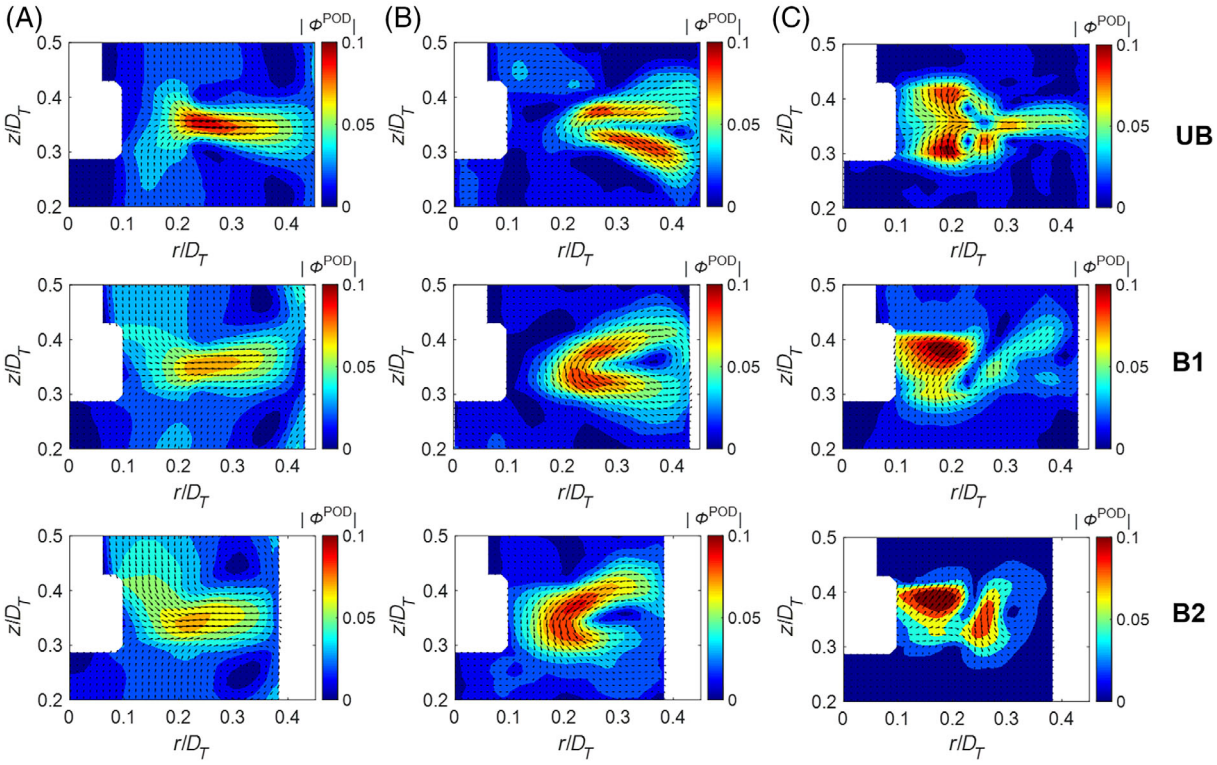

FIGURE 13 Magnitude of the first three POD modes for the three vessel configurations at the plane of measurement P2 (LES dataset): (A) mode 1 ($f_{mean} = 0$ Hz), (B) mode 2 ($f_{UB,LES} = 2.29$ Hz, $f_{B1,LES} = 0.416$ Hz, and $f_{B2,LES} = 0.416$ Hz for the UB and baffled configuration with B1 and B2, respectively), (C) mode 3 ($f_{BPF} = 25$ Hz)

averaged flow field (f_{mean}).[56] In Figure 13C the eigenfunction corresponding to mode 3, with $f_{BPF} = 25$ Hz, for both baffled and UB configurations is representative of the organized flow motion produced by the impeller blade passage. In all configurations the flow associated with mode 3 is characterized by two high energy regions, on opposite sides of the impeller centerline for the UB case, which can be clearly related to the trailing vortices. For the UB and B1 configurations this is more apparent, while for the B2 case the lower trailing vortex region is shifted radially outwards, in agreement with the results presented in Figure 6. Eigenfunctions of mode 2 ($f_{Baffled,LES} = 0.416$ Hz and $f_{UB,LES} = 2.29$ Hz) are illustrated in Figure 13B. The resulting structures indicate the presence of a stream from the tank wall toward the blade region where it sharply turns backwards toward the wall. This stream inverts its direction when there is sign change (i.e., positive or negative) of the corresponding temporal coefficient $\alpha_n(t)$, resulting in a periodic motion from the wall to the impeller centreline. Modes 2 are structurally similar across all the reactor configurations investigated. In the unbaffled vessel the jet structure expands between $r/D_T \sim 0.25$ to $r/D_T \sim 0.4$ introducing a jet oscillation away from the impeller stream (Figure 13B) while with the addition of baffles, this jet structure increases in intensity and moves closer to the impeller suggesting that the tank walls and baffle size play a major role on this organized motion.

To evaluate discrepancies related to the frequency analysis between LES and PIV and assess the nature of the instabilities arising from both datasets, POD was applied to the experimental phase-resolved dataset for the UB and the B1 configurations for different phase angles ($\varphi = 10^\circ - 50^\circ$). The spatial eigenfunction associated with the second mode for the UB and B1 configurations is provided in the first column of Figure 14. From these two plots it is evident that a similar flow structure already identified by the LES POD analysis is also found from the PIV data, with a stream which emanates from the wall toward the impeller region and returns to the tank wall. For the UB-configuration this structure is slightly smaller than the one found from the corresponding LES dataset (cf. Figures 13B and 14A). When the temporal eigenfunctions are considered, mode 2 of the unbaffled-configuration exhibits a dominant frequency in the range of $1.7\,\text{Hz} < f_{UB,PIV} < 2.1\,\text{Hz}$ for all the different phase angles examined $\varphi = 10^\circ - 50^\circ$. This is also in agreement with the frequency, 2.29 Hz found from LES, indicating that the simulations were long enough to capture the time scale of the instability oscillations (4.8 s corresponds to 9–10 cycles) for the UB configuration. For the B1 baffled vessel at the plane of measurement P2, the decomposition resulted in a range of lower frequencies $0.087\,\text{Hz} < f_{B1,PIV} < 0.11\,\text{Hz}$ for $\varphi = 10^\circ - 50^\circ$, which is consistent with the periodicity of fluctuation of β, illustrated in Figures 9 and 10A, C, and E for the same dataset. Therefore, for the B1 configuration the POD analysis applied to the LES results is capable of identifying the spatial flow structure, but due to the limited simulation time the associated frequency is overestimated.

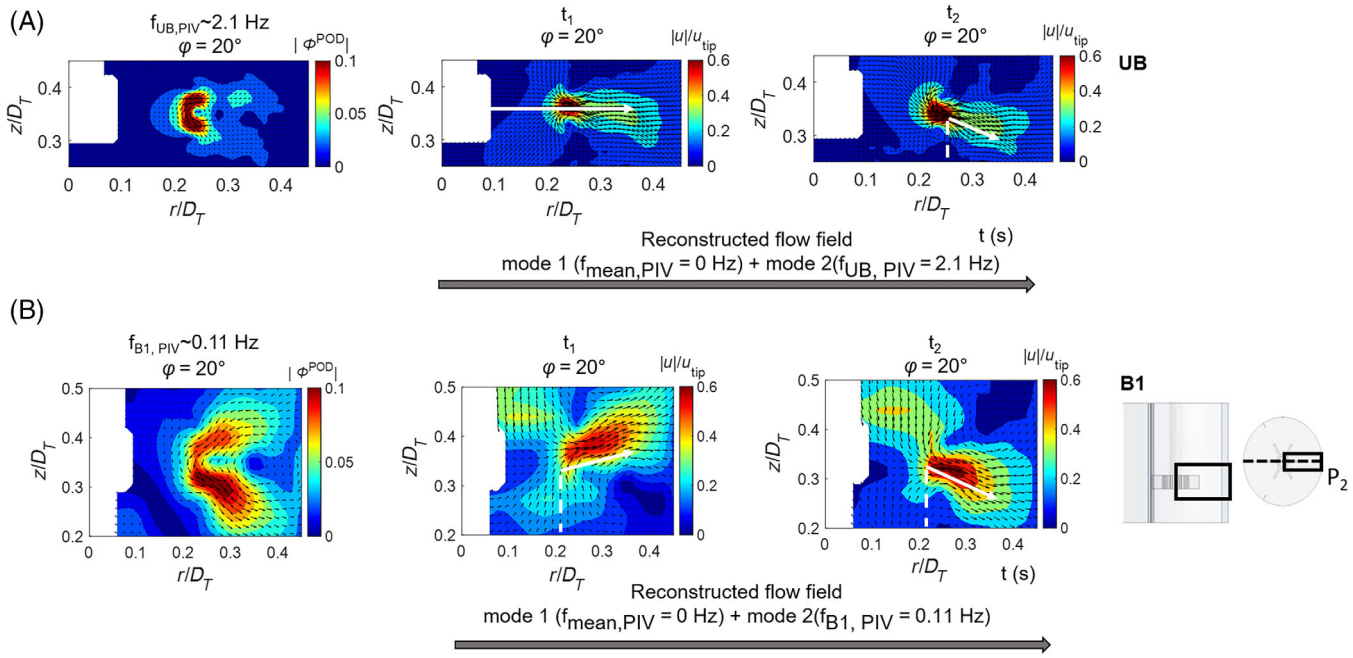

FIGURE 14 Magnitude of the second POD mode (first column) and contours of the reconstructed velocity field (columns 2 and 3) based on PIV phase-resolved dataset ($\varphi = 20^{\circ}$) for the (A) UB and (B) B1 baffled configuration. Flow reconstruction was performed for the (A) UB vessel considering $f(\text{mode } 1, f_{\text{mean}} = 0\,\text{Hz}) + f_{\text{UB,PIV}}\,(2.1\,\text{Hz})$ and (B) B1 vessel considering $f(\text{mode } 1, f_{\text{mean}} = 0\,\text{Hz}) + f_{\text{B1,PIV}}\,(0.11\,\text{Hz})$. The different contour maps for the reconstructed velocity field correspond to two different instants, $t_1 < t_2$

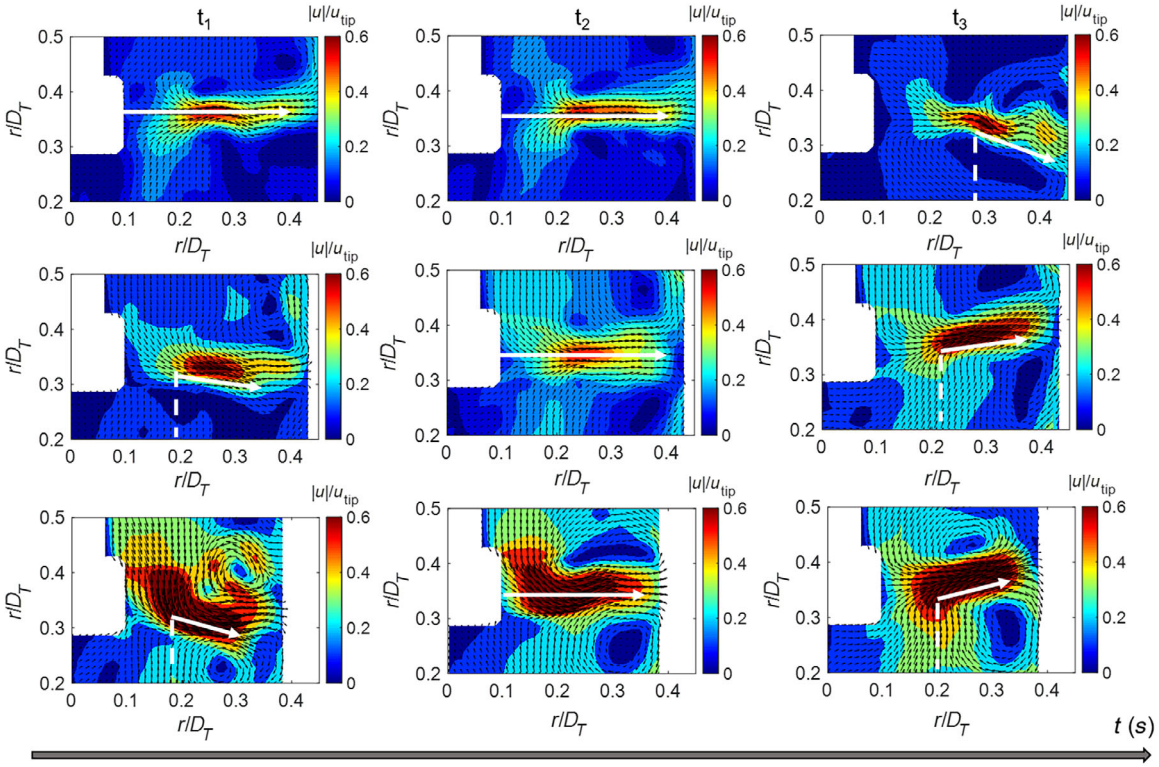

FIGURE 15 Contour and vector maps the instantaneous flow field ($t_1 < t_2 < t_3$) reconstructed with modes containing the two most dominant frequencies. For the UB STR reconstruction was implemented with $f(\text{mode } 1, f_{\text{mean}} = 0\,\text{Hz}) + f_{\text{UB,LES}}(2.29\,\text{Hz})$. For the baffled tanks reconstruction was implemented with $f\,(\text{mode } 1, f_{\text{mean}} = 0\,\text{Hz}) + f_{\text{Baffled,LES}}\,(0.416\,\text{Hz})$

The experimental phase-resolved dataset for UB and B1 was reconstructed following Equation (5) for all the different $\varphi = 10^{\circ} - 50^{\circ}$ considering the temporal modes corresponding to the frequencies associated with mode 2, lying in the range 1.7 Hz < $f_{UB,PIV}$ < 2.1 Hz and 0.087 Hz < $f_{B1,PIV}$ < 0.11 Hz, respectively, and is presented in Figure 14 (for brevity of presentation only $\varphi = 20^{\circ}$ data are presented). Similarly for the simulation data, the flow field in all three configurations (UB, B1, and B2) was reconstructed where the temporal modes embed their corresponding frequencies of $f_{UB,LES} = 2.29$ Hz and $f_{Baffled,LES} = 0.416$ Hz, respectively, and is presented in Figure 15. To identify the effect of the flow structures associated with those frequencies on the average flow field, the first mode, representing the mean flow, was also added in the reconstruction process. The results presented in Figures 14 and 15 corresponding to different instants of the reconstructed flow field showed that, even though the reconstructed velocity field structurally resembled the average flow field due to the higher energy of the first mode (the impeller stream separates the velocity field into two circulation loops), an oscillation of the impeller jet is induced in all configurations. In both experimental and computational data, for the UB reactor, the reconstructed velocity vector plots showed that the impeller stream is quite steady and a downward inclination is induced with $f_{UB,LES} = 2.29$ Hz and $f_{UB,PIV} = 2.1$ Hz, at $r/D_T \sim 0.3$ (Figures 14 and 15). With the addition of baffles the frequency of the jet instability is reduced to $f_{Baffled,LES} = 0.416$ Hz and $f_{B1,PIV} = 0.11$ Hz causing a more intense jet fluctuation with inclination consistent with that one defined in Figure 10 ($\beta \sim 15^{\circ} - 17^{\circ}$).

The results shown in this work are consistent with those of Roussinova et al. who studied the effect of baffles on flow stability and reported large impact on flow periodicity in systems agitated with RTs when number of baffles was reduced from four to three.[20] Additionally in another work Roussinova et al. studied the macroinstabilities inside a baffled tank equipped with a four-blade PBT and reported three factors that can trigger them. The first two are associated with the impingement of the impeller jet on the tank walls and the flow deflection by the baffles whereas the third is linked to the trailing vortices.[57] In their study the impeller clearance was ($C/D_i \sim 0.6$), which is closer to the one used in this work ($C/D_i \sim 0.5$), and it was reported that the flow deflection was a consequence of pressure impingement at the corner of the tank and an imbalance formed between the flow diverted toward the tank wall and that toward the bottom of the tank. The mechanism described by Roussinova et al. can be linked to the jet instability found in this work and can ultimately amplify the effect of flow impingement on the reactor wall creating an oscillating jet which becomes more intense with baffle presence and their increase in size. The reduced stability of trailing vortices may also be attributed to the absence of an impeller disk. In this work and with the current operating conditions ($Re \sim 3,732$) trailing vortices seem to roll up in close proximity to the blades while their radial propagation is minimal compared with traditionally studied cases with a RT.[21,23] Hence, the weak vortex propagation, the operating conditions and the impeller position, are all parameters affecting trailing vortex formation, which may be more pronounced when SDMs are used.

5 | CONCLUDING REMARKS

A systematic characterization of the impact of engineering features and critical design parameters on flow and hydrodynamics in small scale STRs is particularly important for the development of adequately designed SDMs. In this work, the flow dynamics in a scale-down reactor was investigated computationally and validated experimentally. Velocity profiles and turbulence levels were assessed and compared with data available in the published literature for standard reactor designs. Moreover, the impact of the number of baffles and baffle size on velocity and turbulence distributions was presented. Impeller trailing vortices were thoroughly characterized and their stability correlated to baffle presence.

LES investigations were carried out in three scale-down STRs, including one unbaffled and two baffled configurations with different baffle sizes (B1 < B2). Experimental validation, conducted via PIV, showed excellent agreement between simulations and experiments, for both velocity and turbulence distributions, highlighting the reliability of LES models at lower *Re*, where scale-down models tend to operate.

The impact of baffles on hydrodynamics was firstly explored based on velocity and turbulence profiles. The transition from unbaffled to baffled configurations resulted in higher radial and axial velocities due to the abrupt reduction of tangential velocity when baffles are present. Turbulence levels were also amplified as baffles increase the resistance of the system, resulting in an increase in power number.

Trailing vortex formation was thoroughly characterized qualitatively and quantitatively. The stability of the velocity stream was measured by calculating the angle of the impeller jet. In the UB tank, the velocity stream appeared stable, leading to the formation of two distinctive trailing vortices moving in parallel and outwards of the impeller stream. The addition of baffles weakened the parallel vortex motion and induced a periodic oscillation of the angle of the impeller jet corresponding to 37–47 revolutions ($f \sim 0.087 - 0.11$ Hz) and 57–68 revolutions ($f \sim 0.06 - 0.073$ Hz) for the B1 and B2 configurations, respectively. These frequencies could be resolved with PIV experimental data which were long enough to fully capture the instability time scale. The intensity of the vortices was also calculated based on average vorticity values which was denoted by a gradual amplification with increasing baffle size.

To elucidate instabilities affecting trailing vortex formation, spatio-temporal velocity data were processed with POD to find principal modes of variation along with FFT to assign the most prominent frequencies to each mode. Flow decomposition revealed three distinct frequencies associated with the flow stream interacting between the tank wall and impeller flow region. These frequencies correspond to the second most energetic modes and are related to similar flow disturbance effects on the mean velocity flow field. The impact of these periodic flow structures on the mean flow was studied by a LOM comprising only most energetic modes. These reconstructed models clearly indicated the presence of a jet-instability which is amplified in baffled systems, and is associated with a sharp

flow stream emanating from the wall and interfering with the impeller flow region.

The present work contains new information with respect to literature data, on reactor flow field investigation and trailing vortex dynamics characterization. To the best of the author's knowledge, it is the first time a detailed validated hydrodynamic analysis is reported in an already optimized SDM used in continuous bioprocessing and critical design parameters, such as baffle presence and size, are evaluated with regards to their effect on the flow dynamics. Flow sensitivity on the baffle size, indicates the importance of parameter optimization when small-scale STRs are tested and highlights the significance of detailed understanding of the hydrodynamics for optimizing design features.

NOMENCLATURE

BPF	blade passage frequency
CFD	computational fluid dynamics
FFT	Fast Fourier Transform
FBT	flat blade turbine
LES	large eddy simulations
LOM	low order model
MRF	multiple reference frame
TKE	turbulent kinetic energy
PIV	particle image velocimetry
POD	proper orthogonal decomposition
RT	Rushton turbine
SM	sliding mesh
STR	stirred tank reactor
UB	unbaffled
(U)RANS	(unsteady) Reynolds averaged Navier–Stokes equations
P1	vertical plane between baffles
P2	vertical baffle plane

Roman symbols

B (mm)	baffle width
B1	small baffle width ($D_T/16$)
B2	large baffle width ($D_T/10$)
C (mm)	impeller clearance
C_S	Smagorinski constant
D_i (mm)	impeller diameter
d_p (μm)	seeding particle diameter
D_T (mm)	tank diameter
H_L (mm)	liquid height
k' (m^2/s^2)	turbulent kinetic energy
l_o (m)	integral macroscale
N (rpm)	impeller rotational speed
P_0	power number
t_{baffle} (mm)	baffle thickness
t_{blade} (mm)	impeller blade thickness
u_i (m/s)	instantaneous velocity component
$\langle u_i \rangle$ (m/s)	phase resolved velocity component
u_r (m/s)	radial velocity component
u_{tip} (m/s)	impeller tip velocity
u_z (m/s)	axial velocity component
w_b (mm)	impeller blade height

Greek symbols

α_n (m/s)	nth POD temporal eigenfunction
β (°)	angle of the impeller jet
ε (m^2/s^3)	energy dissipation rate
η (m)	Kolmogorov length scale
λ (m)	Taylor microscale
λ_i (m^2/s)	energy of mode i
μ (kg/ms)	dynamic viscosity
ν (m^2/s)	kinematic viscosity
ν_T (kg/ms)	eddy viscosity
ρ (kg/m^3)	density
ρ_p (g/cm^3)	seeding particle density
τ_K (s)	Kolmogorov timescale
Φ_n	nth POD spatial eigenfunction
φ (°)	phase angle
ω (1/s)	vorticity

AUTHOR CONTRIBUTIONS

A. D. Charalambidou: Conceptualization (lead); data curation (lead); formal analysis (lead); investigation (lead); methodology (lead); software (lead); validation (lead); visualization (lead); writing – original draft (lead); writing – review and editing (supporting). **Martina Micheletti:** Funding acquisition (lead); resources (lead); supervision (lead); writing – review and editing (lead). **Andrea Ducci:** Resources (lead); supervision (lead); writing – review and editing (lead).

ACKNOWLEDGMENTS

This work was supported by the Centre for Doctor-al Training (CDT) in Emerging Macromolecular Therapies, Engineering and Physical Sciences Research Council (EPSRC); EP/L015218/1.

DATA AVAILABILITY STATEMENT

The data that support the findings of this study are available from the corresponding author upon reasonable request.

ORCID

Artemis-Danae Charalambidou https://orcid.org/0000-0001-6052-332X

Martina Micheletti https://orcid.org/0000-0001-5147-0182

REFERENCES

1. Alcamo R, Micale G, Grisafi F, Brucato A, Ciofalo M. Large-eddy simulation of turbulent flow in an unbaffled stirred tank driven by a Rushton turbine. *Chem Eng Sci*. 2005;60:2303-2316. doi:10.1016/j.ces.2004.11.017
2. Martínez-Delgadillo SA, Alonzo-Garcia A, Mendoza-Escamilla VX, González-Neria I, Yáñez-Varela JA. Analysis of the turbulent flow and trailing vortices induced by new design grooved blade impellers in a baffled tank. *Chem Eng J*. 2019;358:225-235. doi:10.1016/j.cej.2018.10.015
3. Khan FR, Rielly CD, Brown DAR. Angle-resolved stereo-PIV measurements close to a down-pumping pitched-blade turbine. *Chem Eng Sci*. 2006;61:2799-2806. doi:10.1016/j.ces.2005.10.067

4. Paul K, Herwig C. Scale-down simulators for mammalian cell culture as tools to access the impact of inhomogeneities occurring in large-scale bioreactors. *Eng Life Sci*. 2020;20:197-204. doi:10.1002/elsc.201900162
5. Sandner V, Pybus LP, McCreath G, Glassey J. Scale-down model development in ambr systems: an industrial perspective. *Biotechnol J*. 2019;14:1700766. doi:10.1002/biot.201700766
6. Croughan MS, Konstantinov KB, Cooney C. The future of industrial bioprocessing: batch or continuous? *Biotechnol Bioeng*. 2015;112:648-651. doi:10.1002/bit.25529
7. Steiros K, Bruce PJK, Buxton ORH, Vassilicos JC. Effect of blade modifications on the torque and flow field of radial impellers in stirred tanks. *Phys Rev Fluids*. 2017;2:94802. doi:10.1103/PhysRevFluids.2.094802
8. Kim WJ, Manning FS. Turbulence energy and intensity spectra in a baffled, stirred vessel. *AIChE J*. 1964;10:747-752.
9. Hoseini SS, Najafi G, Ghobadian B, Akbarzadeh AH. Impeller shape-optimization of stirred-tank reactor: CFD and fluid structure interaction analyses. *Chem Eng J*. 2021;413:127497. doi:10.1016/j.cej.2020.127497
10. Wyrobnik TA, Oh S, Ducci A, Micheletti M. Engineering characterization of the novel Bach impeller for bioprocessing applications requiring low power inputs. *Chem Eng Sci*. 2021;117263. doi:10.1016/j.ces.2021.117263
11. Rutherford K, Mahmoudi SM, Lee K, Yianneskis M. The influence of Rushton impeller blade and disk thickness on the mixing characteristics of stirred vessel. *Chem Eng Res Des*. 1996;74:369-378.
12. Van't Riet K, Bruijn W, Smith JM. Real and pseudo-turbulence in the discharge stream from a rushton turbine. *Chem Eng Sci*. 1976;31:407-412. doi:10.1016/0009-2509(76)80024-3
13. Rousseaux J-M, Muhr H, Plasari E. Mixing and micromixing times in the forced vortex region of unbaffled mixing devices. *Can J Chem Eng*. 2001;79:697-707. doi:10.1002/cjce.5450790501
14. Scargiali F, Busciglio A, Grisafi F, Brucato A. Mass transfer and hydrodynamic characteristics of unbaffled stirred bio-reactors: influence of impeller design. *Biochem Eng J*. 2014;82:41-47. doi:10.1016/j.bej.2013.11.009
15. Lamberto DJ, Muzzio FJ, Swanson PD, Tonkovich AL. Using time-dependent RPM to enhance mixing in stirred vessels. *Chem Eng Sci*. 1996;51:733-741. doi:10.1016/0009-2509(95)00203-0
16. Atibeni R, Gao Z. Effect of baffles on fluid flow field in stirred tank with floating particles by using PIV. *Can J Chem Eng*. 2013;91. doi:10.1002/cjce.21652
17. Lu W-M, Wu H-Z, Ju M-Y. Effects of baffle design on the liquid mixing in an aerated stirred tank with standard Rushton turbine impellers. *Chem Eng Sci*. 1997;52:3843-3851. doi:10.1016/S0009-2509(97)88929-4
18. Chapple D, Kresta S. The effect of geometry on the stability of flow patterns in stirred tanks. *Chem Eng Sci*. 1994;49:3651-3660. doi:10.1016/0009-2509(94)00173-1
19. Luo K, Wu F, Yang S, Fan J. CFD–DEM study of mixing and dispersion behaviors of solid phase in a bubbling fluidized bed. *Powder Technol*. 2015;274:482-493. doi:10.1016/j.powtec.2015.01.046
20. Roussinova VT, Grgic B, Kresta SM. Study of macro-instabilities in stirred tanks using a velocity decomposition technique. *Chem Eng Res Des*. 2000;78:1040-1052.
21. Stoots CM, Calabrese RV. Mean velocity field relative to a Rushton turbine blade. *AIChE J*. 1995;41:1-11. doi:10.1002/aic.690410102
22. Escudié R, Liné A. Experimental analysis of hydrodynamics in a radially agitated tank. *AIChE J*. 2003;49:585-603. doi:10.1002/aic.690490306
23. Escudié R, Bouyer D, Liné A. Characterization of trailing vortices generated by a Rushton turbine. *AIChE J*. 2004;50:75-86. doi:10.1002/aic.10007
24. Doulgerakis Z, Yianneskis M, Ducci A. On the manifestation and nature of macroinstabilities in stirred vessels. *AIChE J*. 2011;57:2941-2954. doi:10.1002/aic.12519
25. Roussinova VT, Kresta SM, Weetman R. Resonant geometries for circulation pattern macroinstabilities in a stirred tank. *AIChE J*. 2004;50:2986-3005. doi:10.1002/aic.10275
26. Ducci A, Doulgerakis Z, Yianneskis M. Decomposition of flow structures in stirred reactors and implications for mixing enhancement. *Ind Eng Chem Res*. 2008;47:3664-3676.
27. Ducci A, Yianneskis M. Direct determination of energy dissipation in stirred vessels with two-point LDA. *AIChE J*. 2005;51:2133-2149. doi:10.1002/aic.10468
28. den Akker H, Gillissen JJJ. Spatial distributions of energy dissipation rate in the vicinity of a rushton turbine. MIXING XXIII (NAMF), Mayan Riviera, Mexico; 2012.
29. Micheletti M, Baldi S, Yeoh SL, et al. On spatial and temporal variations and estimates of energy dissipation in stirred reactors. *Chem Eng Res Des*. 2004;82:1188-1198. doi:10.1205/cerd.82.9.1188.44172
30. Tamburini A, Gagliano G, Micale G, Brucato A, Scargiali F, Ciofalo M. Direct numerical simulations of creeping to early turbulent flow in unbaffled and baffled stirred tanks. *Chem Eng Sci*. 2018;192:161-175. doi:10.1016/j.ces.2018.07.023
31. Sarkar J, Kanwar L, Loomba V, Rathore A. CFD of mixing of multiphase flow in a bioreactor using population balance model. *Biotechnol Prog*. 2016;32:613-628. doi:10.1002/btpr.2242
32. Ochieng A, Onyango MS, Kumar A, Kiriamiti K, Musonge P. Mixing in a tank stirred by a Rushton turbine at a low clearance. *Chem Eng Process: Process Intensif*. 2008;47:842-851. doi:10.1016/j.cep.2007.01.034
33. Joshi JB, Sahu AK, Kumar P. LDA measurements and CFD simulations of flow generated by impellers in mechanically agitated reactors. *Sadhana*. 1998;23:505. doi:10.1007/BF02744577
34. Aubin J, Fletcher DF, Xuereb C. Modeling turbulent flow in stirred tanks with CFD: the influence of the modeling approach, turbulence model and numerical scheme. *Exp Therm Fluid Sci*. 2004;28:431-445. doi:10.1016/j.expthermflusci.2003.04.001
35. Delafosse A, Line A, Morchain J, Guiraud P. LES and URANS simulations of hydrodynamics in mixing tank: comparison to PIV experiments. *Chem Eng Res Des*. 2008;86:1322-1330. doi:10.1016/j.cherd.2008.07.008
36. Coroneo M, Montante G, Paglianti A, Magelli F. CFD prediction of fluid flow and mixing in stirred tanks: numerical issues about the RANS simulations. *Comput Chem Eng*. 2011;35:1959-1968. doi:10.1016/J.COMPCHEMENG.2010.12.007
37. Singh H, Fletcher DF, Nijdam JJ. An assessment of different turbulence models for predicting flow in a baffled tank stirred with a Rushton turbine. *Chem Eng Sci*. 2011;66:5976-5988. doi:10.1016/j.ces.2011.08.018
38. de Lamotte A, Delafosse A, Calvo S, Toye D. Identifying dominant spatial and time characteristics of flow dynamics within free-surface baffled stirred-tanks from CFD simulations. *Chem Eng Sci*. 2018;192:128-142. doi:10.1016/j.ces.2018.07.024
39. Hartmann H, Derksen JJ, Montavon C, Pearson J, Hamill IS, van den Akker HEA. Assessment of large eddy and RANS stirred tank simulations by means of LDA. *Chem Eng Sci*. 2004;59:2419-2432. doi:10.1016/j.ces.2004.01.065
40. Gimbun J, Rielly CD, Nagy ZK, Derksen JJ. Detached eddy simulation on the turbulent flow in a stirred tank. *AIChE J*. 2012;58:3224-3241. doi:10.1002/aic.12807
41. Bentolila M, Alshanski I, Novoa R, Gilon C. Optimization of chemical processes by the hydrodynamic simulation method (HSM). *ChemEngineering*. 2018;2:21. doi:10.3390/chemengineering2020021
42. Li F, Hashimura Y, Pendleton R, Harms J, Collins E, Lee B. A systematic approach for scale-down model development and characterization of commercial cell culture processes. *Biotechnol Prog*. 2006;22:696-703. doi:10.1021/bp0504041
43. Nienow AW, Rielly CD, Brosnan K, et al. The physical characterisation of a microscale parallel bioreactor platform with an industrial CHO

cell line expressing an IgG4. *Biochem Eng J*. 2013;76:25-36. doi:10.1016/j.bej.2013.04.011
44. Collignon M-L, Delafosse A, Calvo S, et al. Large-eddy simulations of microcarrier exposure to potentially damaging eddies inside mini-bioreactors. *Biochem Eng J*. 2016;108:30-43. doi:10.1016/j.bej.2015.10.020
45. Tregidgo MB. *Scale-Down Technologies for Perfusion Culture for Rapid Biopharmaceutical Process Development*. University College London; 2021.
46. Smagorinsky J. General circulation experiments with the primitive equations: I. the basic experiment. *Mon Weather Rev*. 1963;91:99-164. doi:10.1175/1520-0493(1963)0912.3.CO;2
47. Gillissen JJJ, den Akker HEA. Direct numerical simulation of the turbulent flow in a baffled tank driven by a Rushton turbine. *AIChE J*. 2012;58:3878-3890. doi:10.1002/aic.13762
48. Zhao J, Gao Z, Bao Y. Effects of the blade shape on the trailing vortices in liquid flow generated by disc turbines, Chinese. *J Chem Eng*. 2011;19:232-242. doi:10.1016/S1004-9541(11)60160-2
49. de Lamotte A, Delafosse A, Calvo S, Toye D. Analysis of PIV measurements using modal decomposition techniques, POD and DMD, to study flow structures and their dynamics within a stirred-tank reactor. *Chem Eng Sci*. 2018;178:348-366. doi:10.1016/j.ces.2017.12.047
50. Weheliye WH, Cagney N, Rodriguez G, Micheletti M, Ducci A. Mode decomposition and Lagrangian structures of the flow dynamics in orbitally shaken bioreactors. *Phys Fluids*. 2018;30:33603. doi:10.1063/1.5016305
51. Liné A. Eigenvalue spectrum versus energy density spectrum in a mixing tank. *Chem Eng Res Des*. 2016;108:13-22.
52. Sirovich L. CFD of mixing of multi-phase flow in a bioreactor using population balance model. *Quart Appl Math*. 1987;45:583-590. doi:10.1090/qam/910463
53. Delafosse A, Morchain J, Guiraud P, Liné A. Trailing vortices generated by a Rushton turbine: assessment of URANS and large Eddy simulations. *Chem Eng Res Des*. 2009;87:401-411.
54. Steiros K, Bruce P, Buxton O, Vassilicos J. Flow field characteristics and energy injection in a tank stirred by regular and fractal blade impellers. In: Segalini A, ed. *Proceedings of the 5th International Conference on Jets, Wakes and Separated Flows (ICJWSF2015)*. Springer; 2016:363-369. doi:10.1007/978-3-319-30602-5_46
55. Lee KC, Yianneskis M. Turbulence properties of the impeller stream of a Rushton turbine. *AIChE J*. 1998;44:13-24. doi:10.1002/aic.690440104
56. Liné A, Gabelle J-C, Morchain J, Anne-Archard D, Augier F. On POD analysis of PIV measurements applied to mixing in a stirred vessel with a shear thinning fluid. *Chem Eng Res Des*. 2013;91:2073-2083. doi:10.1016/j.cherd.2013.05.002
57. Roussinova V, Kresta SM, Weetman R. Low frequency macroinstabilities in a stirred tank: scale-up and prediction based on large eddy simulations. *Chem Eng Sci*. 2003;58:2297-2311.

How to cite this article: Charalambidou A-D, Micheletti M, Ducci A. Study of trailing vortices and impeller jet instabilities of a flat blade impeller in small-scale reactors. *AIChE J*. 2022; e17842. doi:10.1002/aic.17842